Gel Electrolyte Derived from Poly(ethylene glycol) Blending Poly(acrylonitrile) Applicable to Roll-to-Roll Assembly of Electric Double Layer Capacitors

*Cheng-Wei Huang, Ching-An Wu, Sheng-Shu Hou, Ping-Lin Kuo, Chien-Te Hsieh, and Hsisheng Teng**

The synthesis of a gelled polymer electrolyte (GPE) using poly(ethylene glycol) blending poly(acrylonitrile) (i.e., PAN-*b*-PEG-*b*-PAN) as a host, dimethyl formamide (DMF) as a plasticizer and $LiClO_4$ as an electrolytic salt for electric double layer capacitors (EDLCs) is reported. The PAN-*b*-PEG-*b*-PAN copolymer in the GPE has a linear configuration for high ionic conductivity and excellent compatibility with carbon electrodes. When assembling the GPE in a carbon-based symmetric EDLC, the copolymer network facilitates ion motion by reducing the equivalent series resistance and Warburg resistance of the capacitor. This symmetric cell has a capacitance value of 101 F g^{-1} at 0.125 A g^{-1} and can deliver an energy level of 11.5 Wh kg^{-1} at a high power of 10 000 W kg^{-1} over a voltage window of 2.1 V. This cell shows superior stability, with little decay of specific capacitance after 30 000 galvanostatic charge-discharge cycles. The distinctive merit of the GPE film is its adjustable mechanical integrity, which makes the roll-to-roll assembly of GPE-based EDLCs readily scalable to industrial levels.

1. Introduction

Electric double layer capacitors (EDLCs) store electrical energy through the electrostatic interaction of charges at the electrode/electrolyte interface.[1–9] This charge-storage mechanism naturally has a high charge–discharge rate and a long cycle life. To obtain high specific energy and power, the electrodes of EDLCs are made of porous carbon and the electrolytes must have high ionic conductivity.[10–13] However, the long-term stability problems associated with liquid-based EDLCs,[14] and electrolyte leakage in particular, limit their practical application. Developing a gelled polymer electrolyte (GPE) with ionic conductivity comparable to, or even superior to, liquid electrolytes is a solution to these long-term stability issues.

Gelled polymer electrolytes consist of a polymeric framework as the host, an organic solvent as the plasticizer, and a supporting electrolytic salt. Researchers have developed and characterized several polymer hosts for applications in EDLCs[15–24] and lithium-ion batteries,[25–29] including poly(ethylene oxide) (PEO), poly(propylene oxide), poly(vinyl alcohol), poly(vinylidene fluoride), poly(acrylonitrile) (PAN), poly(vinyl chloride), and poly(methyl methacrylate).[30–32] Among these polymers, PAN-based frameworks are widely used in GPEs because they commonly exhibit high cation solvating ability and a wide electrochemical stability window.[30] However, owing to the strong dipole-dipole interacting bonds between the nitrile function groups, PAN has low solubility in most solvents. Dimethylformamide (DMF), which contains a basic nitrogen atom with a lone pair, can penetrate the bonds between the nitrile groups and then swell PAN-containing polymers.

This study reports a copolymer design of PAN blending poly(ethylene glycol) (PEG), i.e., PAN-*b*-PEG-*b*-PAN. The introduction of PEG segments in the copolymer improves the coordination of polymeric framework with solvent molecules,[31,32] which in turn improves the gelation of liquid electrolytes and ion transport in the resulting GPEs. The PAN-*b*-PEG-*b*-PAN was swollen with DMF dissolving $LiClO_4$ as the ion source. The choice of $LiClO_4$ is because this salt has a strong self-dissociation tendency and shows excellent chemical stability and ionic conductivity in PEO- or PEG-based polymer matrices.[33] In this complex, both the polymer matrix and DMF molecule act as the lithium ion-receptor, promoting lithium transport.[34] This resulting GPE has excellent compatibility with carbon electrodes because of its highly-plasticized linear polymer

C.-W. Huang, C.-A. Wu, Prof. S.-S. Hou,
Prof. P.-L. Kuo, Prof. H. Teng
Department of Chemical Engineering and
Research Center for Energy Technology and Strategy
National Cheng Kung University
Tainan 70101, Taiwan
E-mail: hteng@mail.ncku.edu.tw
Prof. C.-T. Hsieh
Department of Chemical Engineering and Materials Science
Yuan Ze Fuel Cell Center
Yuan Ze University
Taoyuan 32023, Taiwan
Prof. H. Teng
Center for Micro/Nano Science and Technology
National Cheng Kung University
Tainan 70101, Taiwan

DOI: 10.1002/adfm.201201342

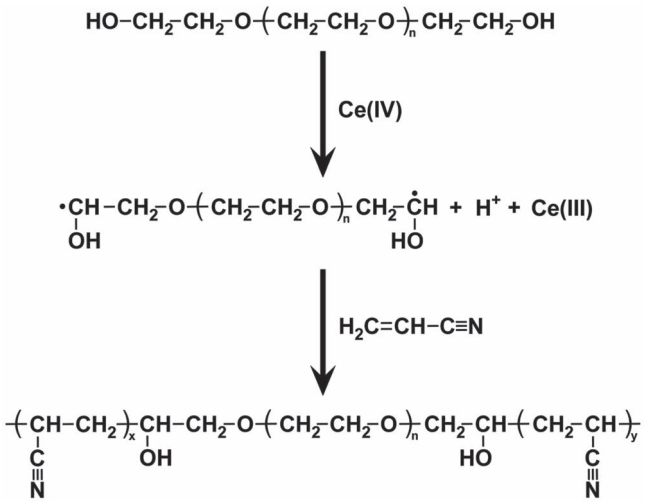

Scheme 1. The synthetic route of the PAN-*b*-PEG-*b*-PAN linear copolymer.

chains. This study demonstrates the superiority of this GPE by analyzing its electrochemical performance and the resulting EDLCs, and presents its mechanical integrity for applicability for roll-to-roll assembly.

2. Results and Discussion

2.1. GPE Structure

Scheme 1 summarizes the PAN-*b*-PEG-*b*-PAN copolymer formation reactions in non-stoichiometric terms, with Ce(IV) as the initiator. Ceric ion redox systems have been extensively used as the initiators for free radical polymerization.[35,36] In the present case of adding vinyl monomers (i.e., AN) to polymers with hydroxyl groups (i.e., PEG), the polymers acted as the reducing agent and reacted with oxidizing Ce(IV) ions to form a complex intermediate, which subsequently decomposed to polymer chain radicals, protons, and Ce(III) ions (see Scheme 1). The radicals then added successive AN monomers to propagate the chain. The chemical formula shown in Scheme 1 reflects the linear feature of the polymer chains.

The PAN-*b*-PEG-*b*-PAN product was obtained by precipitaion with water and acetone. **Figure 1**a shows the scanning electron microscopy (SEM) image of PAN-*b*-PEG-*b*-PAN, depicting the external morphology of the copolymer. The granular structure demonstrates the hydrophobic nature of the polymer formed from an aqueous redox polymerization and subsequent precipitation in water. The granules had a diameter of less than 200 nm. This small size makes the PAN-*b*-PEG-*b*-PAN granules highly accessible to a lithium salt solution, which eventually incorporates into the polymer matrix to form a GPE. Figure 1b shows a photograph of the resulting GPE obtained from heating a $LiClO_4$/PAN-*b*-PEG-*b*-PAN/DMF mixture at 80 °C, followed by casting and evaporating a portion of DMF at 80 °C. This material shows two key properties of solids: mechanical integrity and

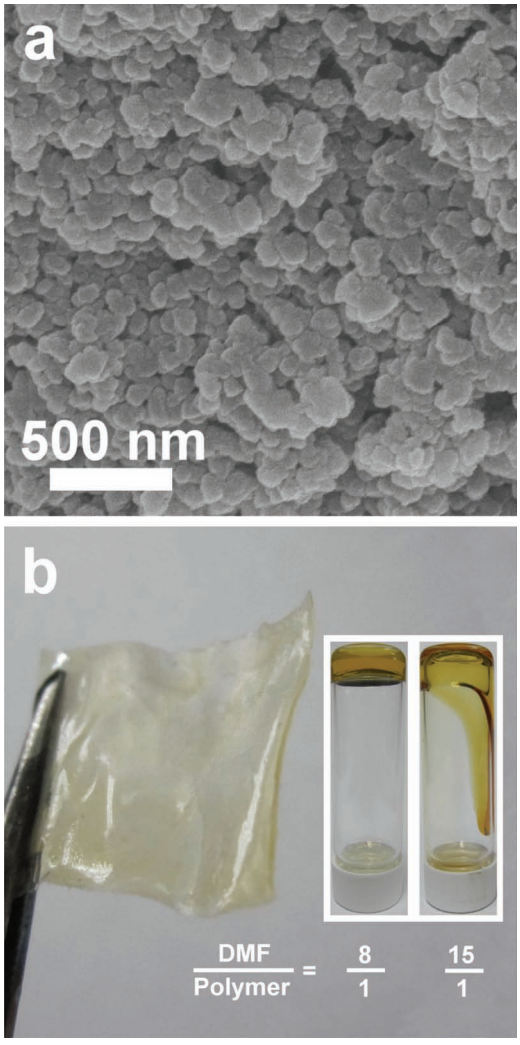

Figure 1. a) SEM image of the PAN-*b*-PEG-*b*-PAN copolymer obtained from precipitaion. b) Photographs of a GPE film obtained from heating a $LiClO_4$/PAN-*b*-PEG-*b*-PAN/DMF mixture at 80 °C for 12 h, followed by casting and evaporating a portion of DMF at 80 °C for 1 h. The inset photographs show the viscous states of the PAN-*b*-PEG-*b*-PAN/DMF gel mixtures with varying DMF contents.

persistent structure. The gel state of the electrolyte varies with the DMF content. The inset photographs of Figure 1b show examples of the copolymer/DMF gel mixtures with different viscous states caused by varying DMF contents. The viscosity of GPEs determines the level of contact between the carbon film and GPE and the EDLC assembly process. This study analyzes the 80 °C-evaporated GPE film.

The ^1H NMR spectrum of the PAN-*b*-PEG-*b*-PAN copolymer (**Figure 2**) reveals a PEG resonance peak at 3.3–3.6 ppm, and those of CH_2 and CH of PAN at 2.0–2.3 and 3.0–3.2 ppm, respectively. Calculating the integrated areas of PEG and PAN segments shows that the polymer chain length of the PAN-*b*-PEG-*b*-PAN copolymer is $(AN)_{563}$-$(EO)_{136}$-$(AN)_{563}$, which corresponds to a molecular weight of 65 500 g mol^{-1}.

Scheme 2 summarizes three interacting modes of solvated Li^+ and ClO_4^- ions with the copolymer and plasticizer and the

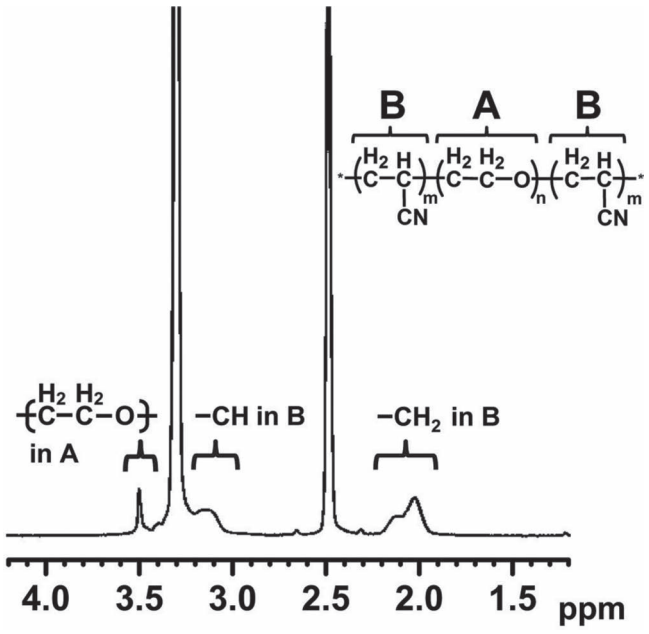

Figure 2. The ^{1}H NMR spectrum of the PAN-*b*-PEG-*b*-PAN copolymer.

various states of the $LiClO_4$ salt in the GPE. Raman spectroscopy confirmed the presence of these interactions in the copolymer–salt complexes. **Figure 3**a shows the Raman spectra of the PAN-b-PEG-b-PAN copolymer and the resulting GPE. The peaks observed at 2960 and 3000 cm^{-1} respectively represent the symmetric and asymmetric C–H stretching vibrations of PAN. The disappearance of the symmetric C–H stretching band at 2960 cm^{-1} upon introducing salt is attributable to the interaction of ClO_4^- anion with the polymer chain, which disturbed the electronic cloud of the C–H bond (Scheme 2a(i/ii)). The copolymer spectrum exhibits a strong stretching peak of free C≡N at 2245 cm^{-1}. The peak intensity of the C≡N band is much lower in the GPE spectrum, indicating extensive interaction between the C≡N group and Li^+ cations or even $[Li^+ClO_4^-]_n$ clusters and plasticizer DMF (Scheme 2a(i/ii)).[37] The copolymer exhibits a C–O–C symmetric stretching vibration peak at 1094 cm^{-1}. This peak shifts to a higher wave number of 1114 cm^{-1} for GPE. The interaction of the ether oxygen with Li^+ cation or solvated Li^+ (Scheme 2a(i/ii)) changed the local conformation of the ether linkage and shifted the peak position.[38]

As for the Raman band contributed directly by the ions, the GPE spectrum in Figure 3a shows the appearance of a strong band of 970–900 cm^{-1} contributed by ClO_4^- anions in different ionic environments.[39–41] This band may include contributions from free ClO_4^- ions at 930 cm^{-1} (Scheme 2b(iii/iv)),[42,43] solvent-shared ions of Li^+–solvent–ClO_4^- at 939 cm^{-1} (Scheme 2a(iii)), contact ion pairs of $Li^+ClO_4^-$ at 948 cm^{-1} (Scheme 2b(i)), and multiple ion clusters of $[Li^+ClO_4^-]_n$ at 955 cm^{-1} (Scheme 2b(ii)).[44] Using Lorentzian curve fitting, Figure 3b shows the decomposition of this ClO_4^- band into the four constituting peaks, where the dotted lines correspond to the simulation results. The intensities of the 948 and 955 cm^{-1} peaks in this figure are low, indicating that the majority of the lithium salt is solvated in GPE.

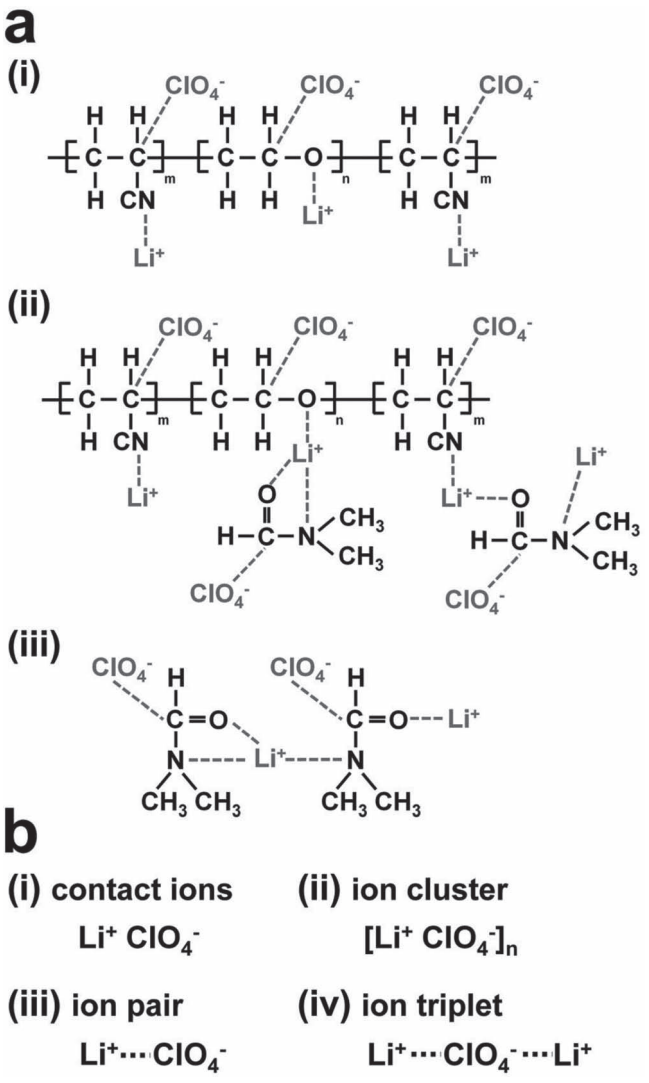

Scheme 2. a) Three interacting modes of solvated Li^+ and ClO_4^- ions with the copolymer and plasticizer in the GPE. b) The various states of the $LiClO_4$ salt in the GPE.

2.2. Electrochemical Properties of Electrolytes

Figure 4 shows the Nyquist plots of AC impedance analysis on GPE, and the liquid-phase $LiClO_4$/DMF and $LiClO_4$/propylene carbonate (PC) electrolyte solutions, which are respectively designated as LE and LE-PC. The loci of the impedance spectra exhibit inclined lines intercepting the Re(Z) axis at high frequencies. The ionic conductivity of the electrolytes was calculated according to

$$k = R_b^{-1} \times S^{-1} \times d \quad (1)$$

where k is the ionic conductivity, R_b is the intercept at the real axis in the impedance Nyquist plot, S is the geometric area of the electrode/electrolyte interface, and d is the distance between the two electrodes. Based on the impedance data, the ionic

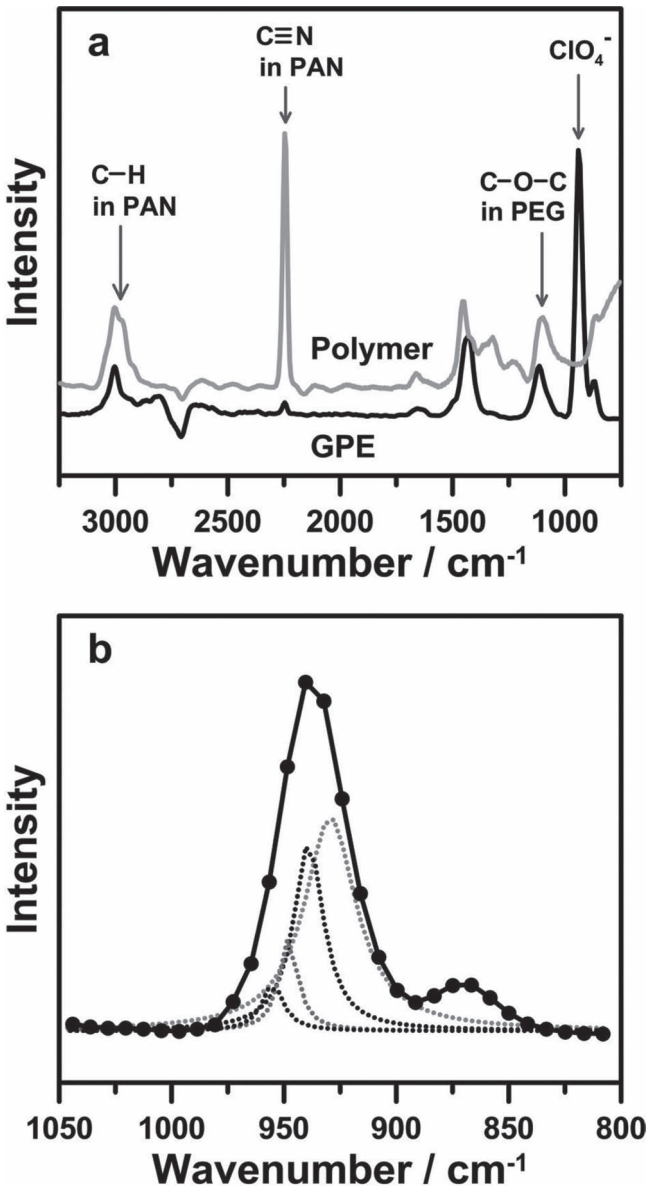

Figure 3. Raman spectra of a) PAN-*b*-PEG-*b*-PAN and the resulting GPE and b) the ClO_4^- anion band in GPE (solid line) and the constituting peaks obtained after spectrum decomposition (dotted lines).

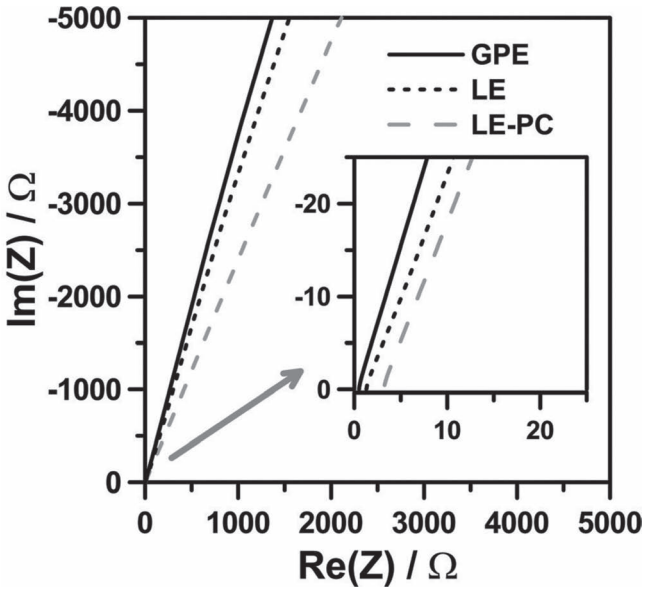

Figure 4. Nyquist impedance plots for GPE, the liquid-phase $LiClO_4$/DMF (LE) and $LiClO_4$/PC (LE-PC) sandwiched by titanium-foil current collectors with frequency ranging from 1 Hz to 100 kHz at an applied potential of 0 V. The inset shows a magnified view of the high frequency region of the impedance spectra.

conductivity values of GPE, LE, and LE-PC were 6.9×10^{-3}, 2.3×10^{-3}, and 9.2×10^{-4} S cm^{-1}, respectively. GPE has a higher conductivity than the two liquid-phase electrolytes. Previous studies synthesized gel electrolytes based on the blend of PAN/PEG swollen with PC or ethylene carbonate dissolving $LiClO_4$ as the ion source.[45,46] These electrolytes exhibited ionic conductivities of $1.2 - 2.5 \times 10^{-3}$ S cm^{-1}, which were lower than that of the present GPE based on the PAN-*b*-PEG-*b*-PAN framework.

The high conductivity of GPE demonstrates the important role of the PAN-*b*-PEG-*b*-PAN matrices and plasticizer DMF in dissociating the $LiClO_4$ salt and facilitating ion motion in the gel electrolyte. The plasticizer molecules soften the polymer backbone and increase segmental motion that produces free volume for transportation of ions through the polymer matrices. Because ion motions are present in both the polymer framework and the solvent channels, the conduction of ions in a gel electrolyte can be swifter than that in the liquid-phase solvent.[14] The Raman spectra of GPE (Figure 3a) show that the PAN and PEG segments of the copolymer strongly interact with the lithium salt for ion solvation (Scheme 2a). On the other hand, the plasticizer DMF reduces the degree of Li^+-assisted polymeric complexation by coordinating Li^+ ions with the oxygen and nitrogen atoms on DMF (Scheme 2a(ii)), and increases the segmental mobility of the polymer. The linear configuration of the copolymer chain, without any cross-linking segments, also increases segmental mobility for efficient ion transport along the polymer chain. Nevertheless, the ion transport caused by the segmental motion of the polymer chains cannot compensate for the transport hindrance caused by the polymer framework. The random sizes of the PEG and PAN segments prevent crystallization of the copolymer and provide interstitial solvent channels for ion transport. The Raman spectrum in Figure 3b shows the presence of free ClO_4^-, solvent-shared Li^+–solvent–ClO_4^- ions, and contact $Li^+ClO_4^-$ pairs and $[Li^+ClO_4^-]_n$ clusters in the free volume of the polymer matrix. The free and solvent-shared ions improve ionic conductivity, while the pairs and clusters exist as an ion reservoir.

The test cells above were analyzed to determine the stable potential window.[13] **Figure 5** shows the cyclic voltammograms of the GPE and LE cells measured at a scan rate of 5 mV s^{-1}. A rise in the current corresponds to the chemical transformation of the electrolytes. By showing the absence of the faradic current due to electrolyte transformation, the voltammograms in this figure indicate that both GPE and LE are stable at potentials between 0 and 2.1 V.

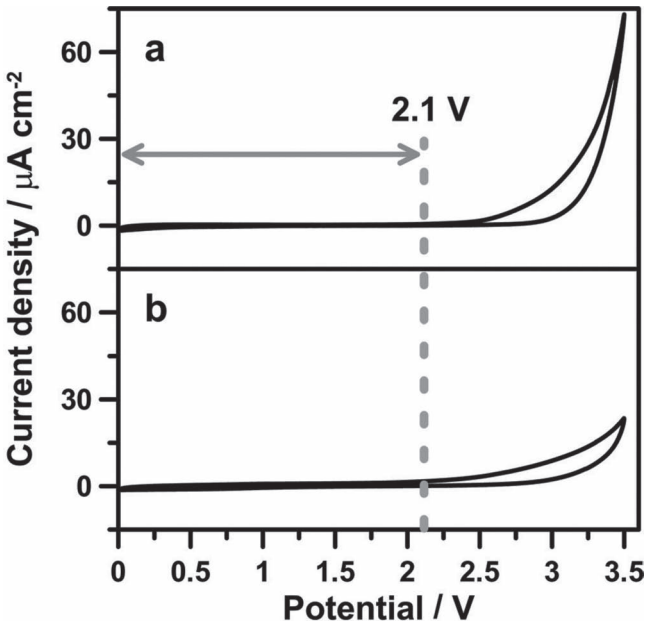

Figure 5. Cylic voltammograms of a) the GPE and b) the liquid-phase electrolyte of $LiClO_4$/DMF (LE) sandwiched by titanium-foil current collectors at a potential scan rate of 5 mV s^{-1}.

2.3. Assembly of Symmetric Cells

Figure 6 depicts the construction of an EDLC cell assembled with GPE. The cell consists of two facing identical carbon electrodes sandwiching a GPE film. The carbon electrodes were wetted with a $LiClO_4$/DMF electrolyte solution before cell assembly. The inset of Figure 1b shows a reduction of GPE viscosity as the DMF content increases. This study also measured the viscosity of GPE at varying DMF/polymer ratios (see Supporting Information). The viscosity decreased exponentially with the increasing DMF content. When the GPE film came in contact with the wetted carbon films under pressure, the boarders of the film became viscous and lost their mechanical integrity due to DMF plasticization. This resulted in the diffusion of the polymer into the carbon film, converting the liquid electrolyte to a gel. This process provided close contact for the carbon/GPE interface. Pre-wetting of the carbon electrodes assured full utilization of the carbon electrode mass in the double layer charge storage, although a polymer concentration gradient may exist in the carbon electrodes. The inset of Figure 6 shows a schematic configuration of the carbon/GPE/carbon sandwich-type cell. While the boarder regions of the GPE film are viscous and well in contact with the carbon particles, the center zone of the GPE film maintains its mechanical integrity and firmly partitions the cell as a separator. Figure 6 demonstrates the feasibility of roll-to-roll assembly of EDLCs using the proposed solid-state GPE. Auxiliary experiments revealed that the contact angles between viscous GPEs and a carbon substrate were small (see Supporting Information), indicating high affinity of viscous GPEs in the carbon film.

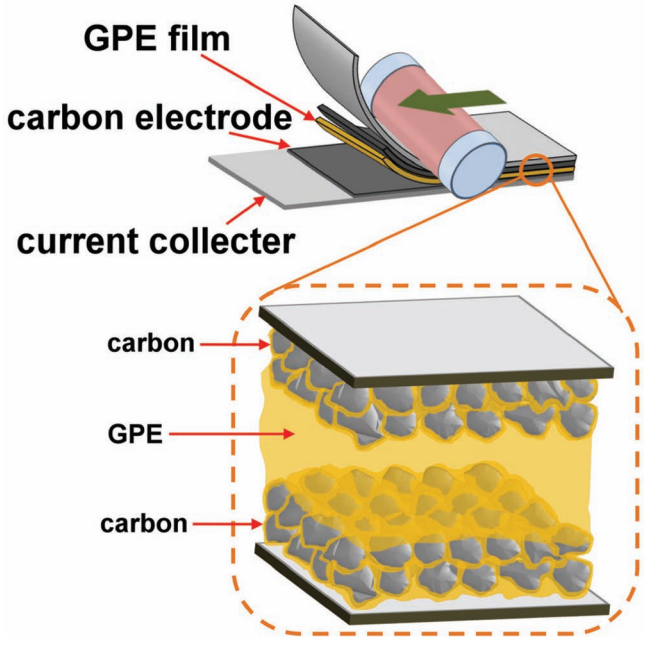

Figure 6. Schematic for the roll-to-roll assembly of an EDLC using the developed GPE film.

The present study analyzed the effect of GPE film thickness, and found that the total resistance of the resultant cells decreased with the decreasing thickness. However, a film thickness of less than 45 μm resulted in shortage of the electrodes in an EDLC. Therefore, the optimal thickness was 50 μm for getting the best performance of EDLCs in the present study. We used this thickness of GPE to assemble EDLCs for performance characterization.

2.4. Electrochemical Capacitive Performance of Resulting Cells

Figure 7 shows cyclic voltammograms of the EDLCs using GPE and LE as the electrolytes at varying scan rates. At a relatively low scan rate of 10 mV s^{-1}, the voltammograms in this figure are nearly rectangular, which is characteristic of an ideal capacitor. With an increase in the potential scan rate, the voltammograms of both GPE-EDLC and LE-EDLC became distorted while the charge transport resistance became a dominant factor. Figure 7 shows that the high-rate voltammograms of GPE-EDLC were less distorted than those of LE-EDLC. These results confirm that GPE is more effective in the charge storage process than LE.

The specific capacitance of GPE-EDLC and LE-EDLC was measured using galvanostatic charge–discharge cycling. The specific discharge capacitance (C) of the electrodes in the EDLC cells was calculated according to

$$C = 4 \times C_{cell} = 4 \times I \times t/(M \times \Delta V) \quad (2)$$

where C_{cell} is the total capacitance of the cell, I is the discharge current, t is the discharge time, M is the total mass of two symmetric electrodes, and ΔV is the potential difference (2.1 V) in discharge. **Figure 8**a shows the specific capacitance values at varying specific discharge currents. The specific capacitance values obtained at the lowest discharge current (0.125 A g^{-1})

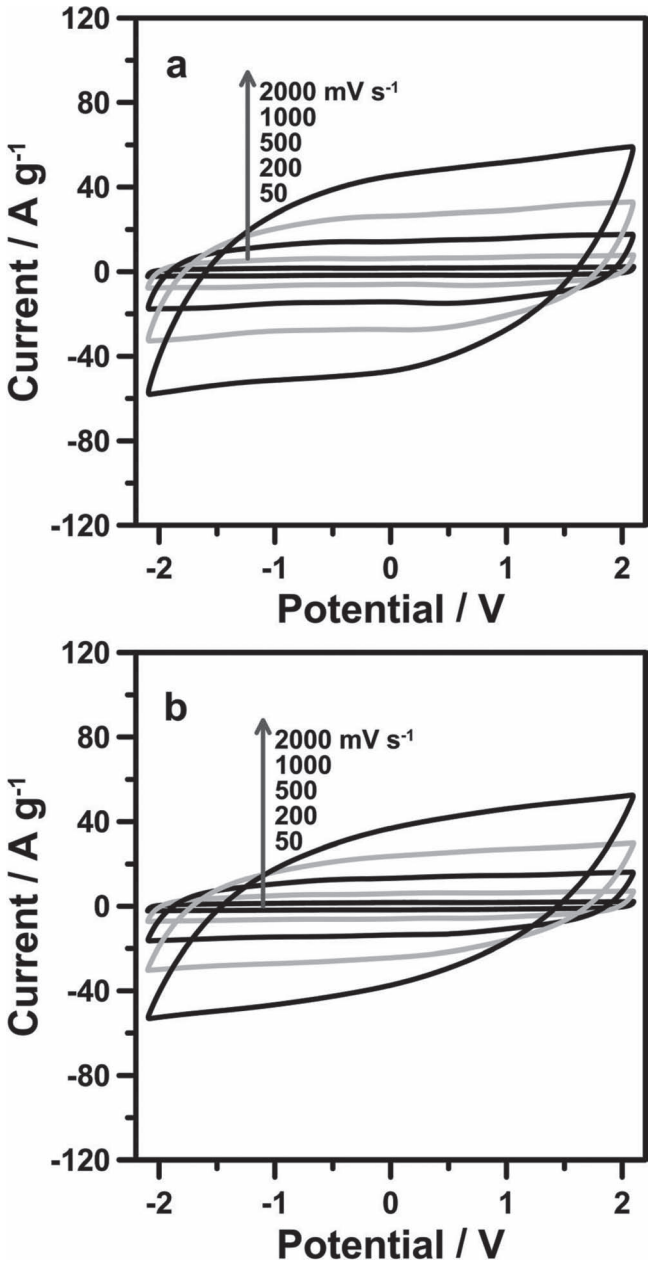

Figure 7. Cyclic voltammograms of symmetric two-electrode capacitors assembled with a) GPE and b) LE as the electrolyte. The electrodes consisted of a 1 cm^2-carbon film (2 mg) and a titanium-foil current collector.

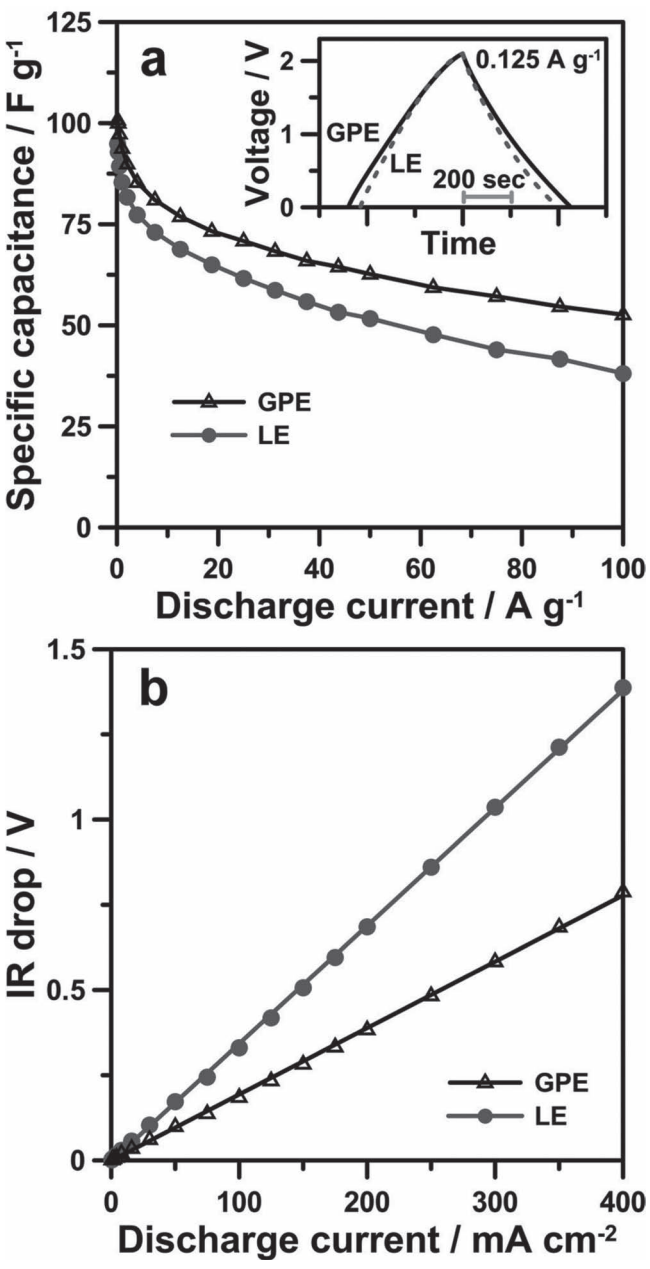

Figure 8. Variation of a) the specific capacitance and b) IR drop with discharge current of the GPE-EDLC and LE-EDLC cells. The inset in (a) shows typical potential vs time curves of the EDLCs charged and discharged at 0.125 A g^{-1}.

are similar, 101 and 95 F g^{-1} for the GPE-EDLC and LE-EDLC electrodes, respectively. The inset of Figure 8a shows the potential-against-time curves of both cells charged and discharged at 0.125 A g^{-1}, exhibiting standard capacitive behavior of double layer capacitors. The capacitance value decreases with the discharge current. This is one of the most important issues in EDLCs. Figure 8a shows that GPE-EDLC has better capacitance retention than LE-EDLC as the current increases. The cell resistance governs the decreasing tendency of the capacitance with the applied current and the overall capacitive performance.[47]

In galvanostatic discharge measurements, an IR (or a potential) drop appears at the beginning of the discharge. This IR drop is associated with the overall resistance (R_t) of the cell. Figure 8b summarizes the variation of the IR drop with discharge current for both cells. The IR drop increases linearly with the discharge current for each cell, and the slope of this linear relationship corresponds to the R_t value. **Table 1** shows that the R_t value of GPE-EDLC is 54% that of LE-EDLC. This difference in resistance explains the higher specific capacitance of GPE-EDLC shown in Figure 8b, and reflects better power performance for GPE-EDLC.

Table 1. Resistance components of the GPE-EDLC and LE-EDLC cells: overall resistance (R_t), equivalent series resistance (R_{es}), equivalent dirtributed resistance for the Warburg region (R_w), and pore resistance (R_p) for electrolyte diffusion, where $R_t = R_{es} + R_w + R_p$.

Electrolyte type	R_t [Ω]	R_{es} [Ω]	R_w [Ω]	R_p [Ω]
GPE	1.9	0.80	0.64	0.50
LE	3.5	1.5	1.4	0.53

To provide a comprehensive perspective on the capacitor performance, this study uses galvanostatic discharge data to correlate the power and energy densities of the cells based on

$$P = I \times \Delta V/(2M) \quad (3)$$

$$E = P \times t_d \left(= C_{cell} \times \Delta V^2/2\right) \quad (4)$$

where P is the power density, E is the energy density, and t_d is the time for complete discharge. **Figure 9** summarizes the P and E results in Ragone plots, showing that the application of GPE improved EDLC performance. The existence of PAN-*b*-PEG-*b*-PAN in the electrolyte preserves the energy at high power density. The energy density can be as high as 11.5 Wh kg^{-1} for the GPE-EDLC cell at a power density of 10 000 W kg^{-1}. In comparison, the energy density was only 9.4 Wh kg^{-1} for LE-EDLC. The PAN-*b*-PEG-*b*-PAN polymeric matrix evidently facilitates charge storage and ionic transport in the cell system. The cells were also analyzed with AC impedance to quantitatively

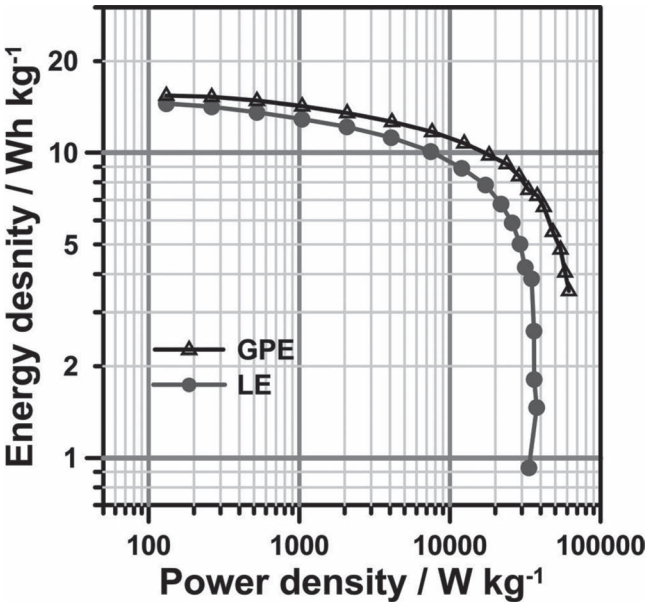

Figure 9. Ragone plots of the GPE-EDLC and LE-EDLC cells with a potential window 2.1 V. Data obtained from the galvanostatic discharge measurement at a current density range of 0.125 A g^{-1} and 100 A g^{-1}.

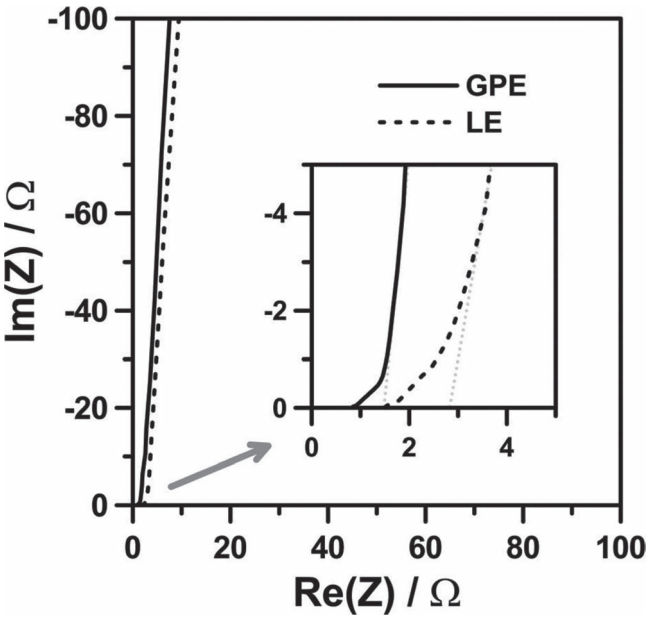

Figure 10. Nyquist impedance plots of the GPE-EDLC and LE-EDLC cells at a frequency range of 10 mHz to 100 kHz and an applied potential of 0 V. The inset shows a magnified view of the high frequency region of the impedance spectra.

characterize the charge storage or transport in each element of the EDLC system.

AC impedance spectroscopy, which distinguishes the resistance and capacitance of devices, revealed the resistance of the capacitor cells in the double layer formation on the carbon electrodes. **Figure 10** shows the Nyquist-type impedance spectra of GPE-EDLC and LE-EDLC scanned at 0 V. The full-scale spectra in this figure contain only vertical lines, indicating that both cells exhibit good capacitive performance. The inset of Figure 10 shows the magnified high-frequency region of the impedance spectra for the cells. The equivalent series resistance (R_{es}) (i.e., the intercept at the Re(Z) axis) was 0.80 Ω (25 kHz) and 1.5 Ω (25 kHz) for the GPE-EDLC and LE-EDLC cells, respectively. The "standard" R_{es} measured at 1 kHz was also obtained for comparison, and yielded values of 0.92 Ω and 1.7 Ω for the GPE-EDLC and LE-EDLC cells, respectively. The R_{es} is primarily associated with the ionic resistance across the partition between the two facing electrodes. The R_{es} values confirm that the PAN-*b*-PEG-*b*-PAN network effectively promotes the ionic motion.

The inset of Figure 10 reveals the presence of a transitional Warburg region at high frequencies before the plot becomes a vertical line. The Warburg region is a result of the distributed resistance/capacitance in the rugged carbon/electrolyte interface region.[47,48] After extrapolating the low frequency straight line to intersect with the Re(Z) axis, the intercept value equals the sum of R_{es} and the equivalent distributed resistance for the Warburg region (R_w). The R_w values of the GPE-EDLC and LE-EDLC cells are 0.64 Ω and 1.4 Ω, respectively. The decrease in R_w is caused by the intimate contact of GPE and carbon particles in the electrode film. The presence of the polymer chains at the carbon/electrolyte interface facilitates the transport of ions toward the pore entrance. Therefore, this GPE reduced the

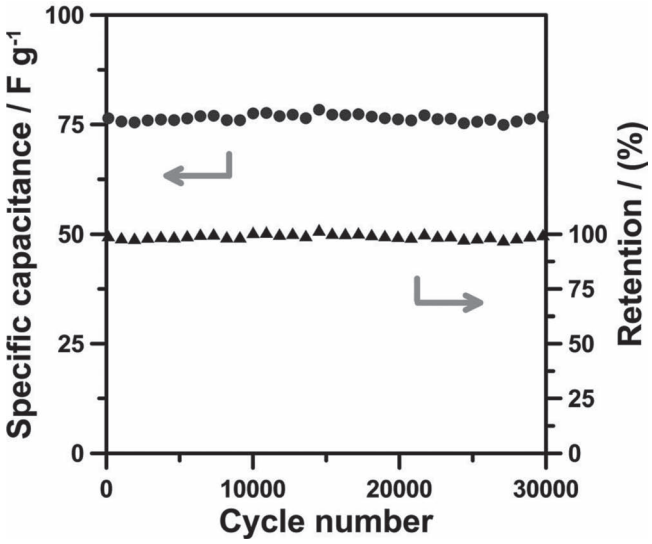

Figure 11. Variation of specific capacitance with cycle number for the GPE-EDLC cell charged and discharged between 0 and 2.1 V at 12.5 A g^{-1}.

cell R_w by 54% compared to LE, enhancing the rate capability of the cell.

The R_t value determined from the IR drop measurements consists of R_{es}, R_w, and electrolyte resistance in the pores (R_p).[3] The R_p value was calculated by subtracting R_{es} and R_w from R_t. Table 1 summarizes the resistance components of the cells. The GPE-EDLC and LE-EDLC cells have similar R_p values because they use the same carbon electrodes. A resistance analysis based on the data in Table 1 indicates that the PAN-*b*-PEG-*b*-PAN network promotes ion motion across the partition zone and through the carbon/electrlyte interface, but leaves the internal diffusion inside pores unaffected.

The GPE-EDLC cell was charged and discharged between 0 and 2.1 V at 12.5 A g^{-1} for 30 000 cycles to test its stability. **Figure 11** shows the variation of capacitance with cycle number. The GPE-EDLC showed negligible decay of specific capacitance after 30 000 cycles. This high cycling stability justifies the repeatability of the double layer formation mechanism facilitated by this chemically stable GPE medium.

3. Conclusions

GPE derived from swelling the PAN-*b*-PEG-*b*-PAN copolymer with a $LiClO_4$/DMF LE exhibits an ionic conductivity of 6.9×10^{-3} S cm^{-1} and mechanical integrity suitable for EDLC assembly at industrial levels. The DMF content controls the GPE viscosity, which in turn affects the contact of the carbon/electrolyte interface and material processing. The high cation-solvating ability of PAN and solvent-coordinating of PEG facilitated efficient transport of the electrolytic ions and solvent molecules in GPE. This led to a low R_{es} of 0.80 Ω for the resulting symmetric GPE-EDLC, while the corresponding LE-EDLC had a R_{es} of 1.5 Ω. The linear configuration of PAN-*b*-PEG-*b*-PAN produces a GPE that is highly compatible with the carbon surface and significantly reduces the ionic resistance in the Warburg region (from 1.4 to 0.64 Ω). The Ragone plot of the GPE-EDLC cell shows outstanding capacitive performance, with an energy density of 11.5 Wh kg^{-1} at a power density of 10 000 W kg^{-1} within a potential window of 2.1 V. Galvanostatic cycling measurements show that the GPE-EDLC has negligible capacitance loss after 30 000 cycles. The use of this gel system not only provides high energy and power densities and long-term stability for EDLC systems, but is also a readily scalable roll-to-roll assembly process.

4. Experimental Section

The PAN-*b*-PEG-*b*-PAN copolymer was prepared by the redox copolymerization of acrylonitrile (Fluka, Switzerland) with PEG (Mn = 6000 g mol^{-1}; Alfa Aesar, UK) at a feed molar ratio (AN/(equivalent OH of PEG)) of 30. The polymerization was carried out in a 8.6 wt% aqueous solution under a nitrogen atmosphere at 40 °C for 6 h using ceric ammonium nitrate (Showa, Japan) as the initiator (the molar ratio of Ce(IV)/equivalent OH of PEG is 2). The product of this polymerization was precipitated with large amounts of deionized water and acetone consecutively for three cycles. The precipitated product was then dried under vacuum at 80 °C for 48 h. The microstructure of the PAN-*b*-PEG-*b*-PAN copolymer was examined with scanning electron microscopy (SEM; JEOL JSM-6700F, Japan).

High-resolution NMR spectroscopy measurements of the PAN-*b*-PEG-*b*-PAN copolymer, dissolved in DMSO, were performed using a Bruker AV-500 spectrometer (Germany) with ^{1}H resonance frequency at 500 MHz. The ^{1}H chemical shifts were referenced relative to tetramethylsilane at 0.0 ppm. Raman spectra of the specimens were recorded at room temperature using a Bayspec Raman spectrometer (USA) with a laser line of 1064 nm. The resolution of Raman measurements was 4 cm^{-1}.

To obtain a GPE film, a homogeneous mixture was formed by heating the mixture of 0.02 g PAN-*b*-PEG-*b*-PAN copolymer, 0.08 g $LiClO_4$, and 0.9 g DMF in a sealed bottle at 80 °C for 12 h. The $LiClO_4$/PAN-*b*-PEG-*b*-PAN/DMF mixture (0.1 g) was then cast onto an aluminum substrate (1.5 cm × 1.5 cm) to evaporate a portion of DMF at 80°C for 1 h. The evaporation time controls the DMF content of the GPE. The resulting GPE film had a DMF/polymer weight ratio of 3.1 and a thickness of 50 μm, and was plastic, transparent, and yellowish. After sandwiching with two titanium foils of 1 cm^2, GPE was analyzed by AC impedance spectroscopy (Zahner-Elecktrik IM6e, Germany) to determine its ionic conductivity. The conductivity measurement was conducted at 0 V with an AC potential amplitude of 5 mV and a frequency range of 1 Hz–100 kHz. Using the same cell setup, we determined the stable potential window of the GPE film with an electrochemical analyzer (Solartron Analytical, Model 1470E, UK). The present study conducted the electrolyte synthesis and device measurements under a nitrogen-purging environment to eliminate the influence from moisture.

The carbon powder used for EDLCs consisted of particulates derived from milling a PAN-based activated carbon fiber cloth (Taiwan Carbon Technology AW1107, Taiwan; 1100 m^2 g^{-1} in surface area) and 5 wt% of multi-wall carbon nanotubes (Aldrich, USA; 10–15 nm in diameter and 1–10 μm in length). Prior to any characterizations or measurements, the carbon powder was heated in a helium atmosphere at 900 °C to remove the surface oxides.

The electrochemical performance of EDLC cells was analyzed using a symmetrical two-electrode capacitor configuration. To prepare the electrodes, the carbon powder (2 mg) was coated on titanium foil with an active area of 1 cm^2 and fixed under stress without using a binder. The symmetrical cell consisted of two facing carbon electrodes, sandwiching a piece of the GPE film. The EDLC cell was assembled under stress to ensure close contact at the carbon–carbon and carbon–Ti foil interface. Cyclic voltammetric characterization of the EDLC cell was conducted within the stable potential window at varying scan rates. The

AC impedance spectroscopy analyzer was employed to measure the impedance behavior of the capacitor cells at 0 V with an AC potential amplitude of 5 mV and a frequency range of 10 mHz to 100 kHz. Cell performance was recorded with an electrochemical analyzer by making galvanostatic charge–discharge measurements for the symmetric cells within the stable potential window with a current density range of 0.125 to 100 A g^{-1}. All electrochemical measurements were carried out at room temperature (≈25 °C).

The ionic conductivity and stable potential window of the electrolytes in cells using a liquid-phase solution as the electrolytes and the capacitive performance of the resulting EDLCs were analyzed for comparison. The liquid-phase cells were assembled in the same manner as for the GPE cells, except that a piece of cellulose paper with a thickness of 30 µm was used to replace the gel film for separating the facing electrodes. The cell was soaked in a concentrated $LiClO_4$/DMF (approximately 4 M, which was optimum for ionic conduction) solution during electrochemical measurements. In addition to the $LiClO_4$/DMF solution, 1 M $LiClO_4$/propylene carbonate was used as an alternative option for liquid-phase electrolytes.[49]

Supporting Information

Supporting Information is available from the Wiley Online Library or from the author.

Acknowledgements

This research is supported by the National Science Council of Taiwan (98-2221-E-006-110-MY3, 101-3113-E-006-010, and 101-3113-E-006-011), the Industrial Technology Research Institute South (B327HK3310), and the Bureau of Energy, Ministry of Economic Affairs, Taiwan (101-D0204-2).

Received: May 17, 2012
Published online: July 3, 2012

[1] K. Kinoshita, *Carbon: electrochemical and physicochemical properties*, John Wiley & Sons, New York **1988**.
[2] B. E. Conway, *Electrochemical supercapacitors: Scientific fundamentals and technological applications*, Kluwer Academic/Plenum, New York **1999**.
[3] S. Yoon, J. Lee, T. Hyeon, S. M. Oh, *J. Electrochem. Soc.* **2000**, *147*, 2507.
[4] P. Simon, Y. Gogotsi, *Nat. Mater.* **2008**, *7*, 845.
[5] M. Heon, S. Lofland, J. Applegate, R. Nolte, E. Cortes, J. D. Hettinger, P. L. Taberna, P. Simon, P. Huang, M. Brunet, Y. Gogotsi, *Energy Environ. Sci.* **2011**, *4*, 135.
[6] K. P. Wang, H. Teng, *Carbon* **2006**, *44*, 3218.
[7] H. C. Huang, C. W. Huang, C. T. Hsieh, P. L. Kou, J. M. Ting, H. Teng, *J. Phys. Chem. C* **2011**, *115*, 20689.
[8] M. D. Strooler, R. S. Ruoff, *Energy Environ. Sci.* **2010**, *3*, 1294.
[9] C. W. Huang, C. M. Chuang, J. M. Ting, H. Teng, *J. Power Sources* **2008**, *183*, 406.
[10] C. W. Huang, C. T. Hsieh, P. L. Kou, H. Teng, *J. Mater. Chem.* **2012**, *22*, 7314.
[11] S. Yoon, S. M. Oh, C. W. Lee, J. W. Lee, *J. Electrochem Soc.* **2010**, *157*, A1229.
[12] M. S. Wu, Y. P. Lin, C. H. Lin, J. T. Lee, *J. Mater. Chem.* **2012**, *22*, 2442.
[13] G. Wang, Z. Shao, Z. Yu, *Nanotechnology* **2007**, *18*, 205705.
[14] M. Ishikawa, M. Morita, M. Ihara, Y. Matsuda, *J. Electrochem. Soc.* **1994**, *141*, 1730.
[15] C. P. Tien, W. J. Liang, P. L. Kuo, H. Teng, *Electrochim. Acta* **2008**, *53*, 4505.
[16] C. P. Tien, H. Teng, J. Taiwan *Inst. Chem. Eng.* **2009**, *40*, 452.
[17] C. P. Tien, H. Teng, *J. Power Sources* **2010**, *195*, 2414.
[18] H. Gao, K. Lian, *J. Power Sources* **2011**, *196*, 8855.
[19] Y. Ding, F. H. Meng, *Adv. Mater.* **2011**, *23*, 4098.
[20] G. Wee, O. Larsson, M. Srinivasan, M. Berggren, X. Crispin, S. Mhaisalkar, *Adv. Funct. Mater.* **2010**, *20*, 4344.
[21] M. Kaempgen, G. K. Chan, J. Ma, Y. Cui, G. Gruner, *Nano Lett.* **2009**, *9*, 1872.
[22] C. Meng, C. Liu, L. Chen, C. Hu, S. Fan, *Nano Lett.* **2010**, *10*, 4025.
[23] G. P. Pandey, S. A. Hashmi, Y. Kumar, *J. Electrochem. Soc.* **2010**, *157*, A105.
[24] M. Morita, J. L. Qiao, N. Yoshimoto, M. Ishikawa, *Electrochim. Acta* **2004**, *50*, 837.
[25] N. Wu, Q. Cao, X. Wang, X. Li, H. Deng, *J. Power Sources* **2011**, *196*, 8638.
[26] H. Li, X. T. Ma, J. L. Shi, Z. K. Yao, B. K. Zhu, L. P. Zhu, *Electrochim. Acta* **2011**, *56*, 2641.
[27] Y. T. Chen, Y. C. Chuang, J. H. Su, H. C. Yu, Y. W. Chen-Yang, *J. Power Sources* **2011**, *196*, 2802.
[28] H. R. Jung, W. J. Lee, *Electrochim. Acta* **2011**, *58*, 674.
[29] M. Deka, A. Kumar, *Electrochim. Acta* **2010**, *55*, 1836.
[30] A. M. Stephan, K. S. Nahm, *Polymer* **2006**, *47*, 5952.
[31] J. Y. Song, Y. Y. Wang, C. C. Wan, *J. Power Sources* **1999**, *77*, 183.
[32] A. M. Stephan, *Eur. Polym. J.* **2006**, *42*, 21.
[33] R. Subadevi, M. Sivakumar, S. Rajendran, H. C. Wu, N. L. Wu, *J. Appl. Polym. Sci.* **2011**, *119*, 1.
[34] W. Wieczorek, G. ukowska, R. Borkowska, S. H. Chung, S. Greenbaum, *Electrochim. Acta* **2001**, *46*, 1427.
[35] W. C. Hsu, J. F. Kuo, C. Y. Chen, *J. Polym. Sci. Part A: Polym. Chem.* **1992**, *30*, 2459.
[36] W. C. Hsu, C. Y. Chen, J. F. Kuo, E. M. Wu, *Polymer* **1994**, *35*, 849.
[37] H. W. Chen, F. C. Chang, *J. Polym. Sci. Part B: Polym. Phys.* **2001**, *39*, 2407.
[38] K. V. Ramana, S. Singh, *Spectrochim. Acta, Part A* **1988**, *44*, 277.
[39] D. W. James, R. E. Mayes, *Aust. J. Chem.* **1982**, *35*, 1775.
[40] R. L. Frost, D. W. James, R. Appleby, R. E. Mayes, *J. Phys. Chem.* **1982**, *86*, 3840.
[41] S. Selvasekarapandian, R. Baskaran, *Spectrochim Acta Part A* **2006**, *65*, 1234.
[42] D. Battisti, G. A. Nazri, B. Klassen, R. Aroca, *J. Phys. Chem.* **1993**, *97*, 5826.
[43] Y. Chatani, S. Okamura, *Polymer* **1987**, *28*, 1815.
[44] Z. Wang, B. Huang, S. Wang, R. Xue, X. Huang, L. Chen, *J. Electrochem Soc.* **1997**, *144*, 778.
[45] B. K. Choi, Y. W. Kim, K. H. Shin, *Electrochim. Acta* **2000**, *45*, 1371.
[46] Y. H. Liang, C. C. Wang, C. Y. Chen, *J. Power Sources* **2008**, *176*, 340.
[47] C. W. Huang, C. H. Hsu, P. L. Kuo, C. T. Hsieh, H. Teng, *Carbon* **2011**, *49*, 895.
[48] C. W. Huang, H. Teng, *J. Electrochem. Soc.* **2008**, *155*, A739.
[49] D. Aurbach, I. Weissman, *Nonaqueous Electrochemistry* (Ed: D. Aurbach), Marcel Dekker, New York **1999**, Ch. 1.